SUPPLEMENTARY DOCUMENT

TITLE:
Experimental Methods for Trapping Ions Using Microfabricated Surface Ion Traps

AUTHORS & AFFILIATIONS:
Seokjun Hong[1] (sjhong84@snu.ac.kr);
Minjae Lee[1] (mjlee88@snu.ac.kr);
Yeong-Dae Kwon[2] (ykwon@sk.com);
Dong-il "Dan" Cho[1] (dicho@snu.ac.kr)
Taehyun Kim[2] (quantum@sk.com);
[1]ISRC/ASRI, Department of Electrical and Computer Engineering, Seoul National University, Republic of Korea
[2]Quantum Tech. Lab, SK Telecom, Republic of Korea
Correspondence to: Taehyun Kim

S.1. Packaging of the ion trap chip

There are a few different alternatives to install the chip inside an ultra-high vacuum (UHV) chamber[1-3]. Among them, this paper explains an approach where the chip is glued on a separate chip carrier. This chip carrier is inserted into a zero-insertion-force (ZIF) socket on a printed circuit board (PCB)[4]. A procedure to mount the fabricated trap chip on a chip carrier is explained in this section. Note that a procedure to build a UHV chamber with a ZIF socket is explained in S.2.

In the method using a chip carrier and a ZIF socket, the chip is mounted on a chip carrier and electrically connected to the chip carrier by gold bonding wires. The chip carrier should be compatible with a baking process and UHV environment, and ceramic chip carriers with gold electrodes are typically used. Especially in the case that the system is designed to load neutral atoms from the backside of the trap chip, a loading hole is fabricated at the center of the chip carrier. In this paper, a 3-mm-diameter hole was fabricated by using a conventional drilling press. The chip carriers commonly used in surface-ion-trap applications have a cavity to hold the chip such that the surface of the chip is recessed compared to the chip carrier body. In this case, interposer chips should be inserted under the trap chip to allow the laser beams to access the trapping position right above the chip. The interposer chip can be easily fabricated by cutting a bare silicon wafer with an appropriate thickness into pieces. Two silicon spacers can be glued on the chip carrier using a UHV-rated epoxy compound, with aligning the loading hole fabricated at the center of the chip carrier between the spacers. Then, the ion-trap chip is glued on top of the silicon spacers using the same UHV-rated epoxy. The bonding wires can also interfere with propagation of the laser beam. To avoid this, the layout of the bonding pads should be designed considering the beam paths in the layout design step. Alternatively, a low-loop wire bonding method can be used. Also, the increased height of the overall chip due to the interposer chip and the bonding wires should be taken into account during the chamber design stage.

S.2. Design and construction of ultra-high vacuum chamber

An overall design of a UHV chamber is shown in **Figure S1**. The ion pump can lower the

pressure down to 10^{-10} Torr range, but to reach a pressure below $3x10^{-11}$ Torr, a non-evaporable getter (NEG) pump is added. The trap chip package is installed in a spherical octagon and all experiments are performed around this spherical octagon. In addition to maintaining a UHV pressure, the in-vacuum components in the spherical octagon should be designed to accommodate as many laser beam paths as possible and also to allow an imaging lens to be placed as close as possible to the chip surface in order to achieve high resolution imaging of the trapped ions with a diffraction-limited, high numerical aperture (NA) lens. **Figure S2(a)** illustrates the internal structure of the spherical octagon which allows easy installation and removal of the trap chip package.

One of the common challenges in construction of the chamber is to make an efficient oven for neutral ytterbium (Yb) atoms and the oven holder. They should be designed to minimize heat conduction without compromising mechanical stability. In this section, a design of Yb oven is described, and an effective method to test the oven is explained. In addition, the design of the other components in the spherical octagon and testing procedures are provided.

Figures S2(b) and (c) show the construction of ovens for neutral Yb. Two metal tubes of 1 mm diameter are cut into a length of 20 mm, and one end of each tube is bent to seal that end. One tube is filled with a small piece of naturally occurring Yb and another tube is filled with isotopically enriched ^{171}Yb. To prevent the small Yb pieces from falling off from the tube, the middle of each tube is squeezed slightly in two orthogonal directions along the tube as shown in **Figure S2(b)**. A 30-mm-long tantalum strip with a width of 0.5mm is used as a filament to heat the oven. One end of the tantalum strip is spot-welded to the bent end of the tube, and the other end is spot-welded to a Kapton-insulated copper wire as shown in **Figure S2(b).** The open ends of the tubes are fastened to an oven holder with a set screw as shown in **Figure S2(c)**. The Kapton wires are inserted into the wire threading holes in the oven holder to prevent an accidental short circuit between metal parts of the chamber and the filament which can be easily contorted from thermal stress or mechanical shock. Because the tantalum filament can also be evaporated in a high temperature and the evaporated tantalum can short the traces on the PCB, a protective screen is placed between the PCB and the oven supporting layer.

To find the minimum current which leads to evaporation of the Yb ovens, a common approach is to put a slide glass in front of the oven in the chamber, and wait until the transparency of the glass changes by the coated metal. Unfortunately, this method is not reliable for a small change in transparency. In our setup, a residual gas analyzer (RGA) is used to detect the evaporation of Yb atoms. The RGA is temporarily attached to the front 6" conflat (CF) flange of the spherical octagon, and **Figure S3** shows that the measurement result with RGA agrees with the expected distribution of the Yb isotopes.

For easy installation and removal of the chip carrier, a ZIF socket[4] is mounted on the PCB board as shown in **Figure S2(a).** All electrical connections on the PCB board are made using press-fit type pins and press-fit type pin sockets to avoid the use of solder in the UHV environment. **Figure S2(a)** also shows a grounded metal shield between the trap chip package and the recessed viewport to minimize potential disturbance from any stray charges trapped on the front viewport.

Before and after the chamber baking, two types of electrical tests are performed to make sure that there is no electrical problem. (The baking process is separately described in S.3.) To check for any accidental short circuit among electrodes of the ion trap chip, the resistance

among the corresponding pins of feedthroughs are measured. To verify the continuity of the electrical connections between all the electrodes and the corresponding pins of feedthroughs, capacitance between each pin and the ground is also measured.

S.3. Details of baking process

To reach a UHV pressure, the entire chamber needs to be baked, and **Figure S4** shows one exemplary log of the baking process. Before being baked, the chamber was pumped down with a turbo pump until the pressure reached 10^{-6} Torr range, which generally takes one day. During this period, we performed a leak test and outgassed the Yb ovens, ion gauge and NEG pump. After that, the temperature of the chamber was increased to 200°C at a rate of 0.2°C/min. As the temperature goes up, the pressure starts to increase, but the pressure generally starts to drop in the middle of the ramping process. The log in **Figure S4** shows only the pressure data collected from the fourth day after the baking process was started. An ion pump was turned on after the pressure reached the bottom saturation point, and the baking was continued for a few more days. The temperature was ramped down at a rate of 0.2°C/min, and when the temperature reached room temperature, the NEG pump was activated. To activate the NEG pump, the activation voltage was gradually increased in many steps until it reached the manufacture's recommended value (16V, 5.5A) and that value was maintained for an hour. During this activation process, generally severe outgassing was observed, and the ion pump and ion gauge were switched off when the pressure went above 10^{-5} Torr. Even after the activation, the effects of getter outgassing remained for a long time, and additional baking for a few days was helpful to reach the desired UHV pressure quickly. During this second baking, disconnecting the chamber from the turbo pump can also be helpful to reach a lower pressure. Our ion gauge was housed inside a 2.75" CF tee, and the temperature of the tee surrounding the ion gauge was higher than the rest of the chamber because of the heat generated by the ion gauge filament. To minimize any bias coming from local heating during the pressure measurement, the tee surrounding the ion gauge was cooled after measuring the final chamber pressure.

S.4. Laser parameters used for trapping $^{174}Yb^{+}$ ions

Given a surface trap, there are many possible configurations of beam paths and beam parameters that can lead to successful trapping of ions. In this section, the parameters used in our setup are explained, but the readers should choose an appropriate configuration that suits their specific setup.

In our $^{174}Yb^{+}$ ion trap setup, the main function of the 369.5 nm laser is Doppler cooling of the Yb ions. A typical ion trap experiment uses a single beam path, so to cool the motion of the ions along all three principal axes of the total potential, the beam path is chosen to be not orthogonal to any of three principal axes so that the momentum vector of the absorbed photons has non-zero components along all three principal axes. **Figure 8** shows a fictitious beam path whose momentum vector has a component along the axial direction (*z*-axis) of the trap geometry and also an orthogonal component along *x*-axis. If symmetric voltages are applied to the direct current (DC) electrodes, one of the principal axes will be parallel to the *y*-axis, but this is orthogonal to the momentum vector of the laser so the cooling efficiency along this axis will be compromised. To avoid this problem, two principal axes in the radial direction (*xy*-plane) are tilted with respect to the geometry of the chip by applying asymmetric voltages similar to **Figure 4**. In our setup, the surface trap chip is mounted at a

45° angle with respect to the optical table so that the beam path of the cooling laser can be set parallel to the optical table.

In our setup, 935nm and 399nm lasers are set to co-propagate from the opposite side of the chamber as shown in **Figure 5**, but there are also many other ways to set the laser paths. The first factor to consider is the orientation of the magnetic field and the polarization of the laser that depend on the selection rule. Other factors to consider include the imaging scheme, scattering from the bonding wires, spatial constraints coming from the chamber dimension, availability of proper optical components, convenience of the optical setup, and plans for future experiments. For example, one way to make all three lasers meet at the trapping position is to combine all the beams parallel to each other with some space, and focus them together using a single achromatic lens. However, in our setup, co-propagating setup was chosen because of the unavailability of an achromatic lens with proper anti-reflection (AR) coating and the focal length suitable for our vacuum chamber design and chip dimension.

The desired beam waists of all the lasers were first calculated to minimize the beam clipping from the edge of the trap chip[5], and then the actual sizes were selected by considering focal lengths of the commercially available lenses. For example, when the half size of the chip is 5 mm, the ideal beam waist (w_0) of 369.5 nm laser is 24 μm. In one of our experimental setups, the output of the 369.5 nm fiber has a beam waist of w_0 = 1.54 μm, and it is first collimated to a beam waist of ~ 870 μm by an ultraviolet (UV) collimator. Then it is focused down to w_0 ~ 26 μm by a singlet lens as shown in **Figure 5**. The output from the 399 nm fiber has a beam waist of 1.82 μm, which is collimated to a beam with w_0 ~ 800 μm by the same type of UV collimator. Then it is focused down to w_0 ~ 20 μm by a singlet lens shared with the 935 nm laser as shown in **Figure 5**. The output from the 935 nm fiber has a beam waist of 3.4 μm, and it is collimated to a beam with w_0 ~ 750 μm by the infrared (IR) collimator. Then the collimated 935 nm beam is focused down to w_0 ~ 60 μm by the shared singlet lens. Note that these numbers represent just one case, and other numbers can also be chosen for different setups.

When the alignments of all the lasers are fully optimized, a single ion can be trapped with less than 2 μW of the 369.5 nm laser with red detuning of 10 MHz because the peak intensity (188 mW/cm^2) is much larger than the saturation intensity[6] (51 mW/cm^2). However, because of the large detuning of the laser and large uncertainty in the alignment during the initial trapping described in step 2.4, we generally used 2 mW of the 369.5 nm laser red-detuned by 200 MHz to maximize the chance of initial trapping, and after optimization, we reduce the power to a necessary level for a given detuning. For the same reason, we used 4 mW of the 935 nm laser and 1 mW of the 399 nm laser which are several orders of magnitude larger than the corresponding saturation intensity for the initial trapping.

A $^{174}Yb^+$ ion has two Zeeman sublevels ($|J = 1/2, m_J = \pm 1/2\rangle$) at both $^2S_{1/2}$ state and $^2P_{1/2}$ state which can be pumped into a dark state with a circularly polarized laser[7]. In general, the polarization of the light delivered through an optical fiber becomes elliptical unless it is carefully controlled, and it also changes over time. Therefore, there will be non-zero components of both left- and right-circularly polarized lights in general and even when the propagation direction of the laser is parallel to the B-field, perfect optical pumping into a dark state will not happen automatically. On the other hand, the overall cooling efficiency will be limited by the smaller portion of the two circularly polarized components, and to maximize the cooling efficiency, the polarization needs to be controlled. However, if the B-

field is perpendicular to the propagation direction of the laser, both parallel and perpendicular components of polarization with respect to the B-field contribute to the cooling and the cooling efficiency becomes almost insensitive to the polarization of the laser especially when the detuning is much larger than the Zeeman splitting for initial trapping. **Figure 6(a)** shows a coil installed at the front of the chamber to generate a B-field that is nearly perpendicular to the surface of the chip in our setup. In this configuration, the propagation directions of all the lasers are perpendicular to the B-field, and the cooling efficiency will be independent of the polarization of the 369.5 nm laser, but to get the maximum re-pumping efficiency of the 935 nm laser, it is important to have non-zero perpendicular polarization component of the 935 nm laser with respect to the B-field because the parallel polarization can drive only π transitions between $^2D_{3/2}$ and $^3D[3/2]_{1/2}$ and the ion can be optically pumped into $^2D_{3/2}|J = 3/2, m_J = \pm 3/2\rangle$. Note that this is one example configuration, and the directions of the B-field and polarizations should be chosen based on specific experiments.

Our wavelength meter is regularly calibrated to one of the strong crossover lines of 85 Rubidium (^{85}Rb) D2 transition. The absolute accuracy specified in the datasheet of our wavelength meter is 19 MHz at 399 nm, and our measured frequency of ^{174}Yb $^1S_0 \leftrightarrow {}^1P_1$ transition is roughly 70 MHz different from 751,526,533.49(33) MHz given by Kleinert *et al.*[8]. We believe the main reason for the difference is Doppler shift and broadening coming from non-orthogonal direction of the oven with respect to the beam path.

S.5. Design consideration for imaging setup

To maximize the collection efficiency of the emitted photons from the trapped ion, an imaging lens with high NA and a custom-made recessed viewport are used as shown in **Figure 5** and **Figure 6(c)**. The imaging lens has NA of 0.6 and AR coating for 369.5 nm and it is designed to be diffraction-limited at 369.5 nm. The expected magnification of the lens was 8.6 from the numerical simulation, and it was confirmed by the actual measurement of 8.9(1) which was obtained by comparing the image size of electrodes in **Figure 8** and the mask design of the ion trap chip. We believe the difference was caused by the non-optimal alignment of the imaging system.

The working distance is 17.2 mm including 4-mm thick viewport, and if different thickness of viewport is chosen, the simulation shows that it becomes difficult to achieve diffraction-limited resolution. **Figure S2** shows that our system is composed of multiple components, and the height of each component has some amount of uncertainty. The depth of the recessed viewport is determined considering the amount of inaccuracies in fabrication and assembly.

S.6. Experimental setup for manipulation of $^{171}Yb^+$ ions

Depending on the final goal of the experiment, there are a few different options for the control system. For example, trapping of $^{174}Yb^+$ ions can be achieved by using several variable DC power supplies for the DC electrodes and adjusting the wavelengths of all the lasers manually. However, to manipulate and detect $^{171}Yb^+$ hyperfine qubits, multiple electrical and optical components should be controlled at sub-microsecond timing, and therefore, it is recommended to build a dedicated control system[9]. In our experimental setup, multiple DC voltages were generated by a commercial digital-to-analog converter (DAC) board that is directly controlled by a computer. In the future, to synchronize the

location of the ions with more complex sequences of optical controls it will be replaced by a home-built DAC board with 96 output channels, controlled by a field-programmable gate array (FPGA). To minimize the electrical noise coupled through the DC voltage lines, small filter boards are directly connected to the air side of the 6" CF flange with four sub-D feedthroughs shown in **Figure S2**. Each board has 23~25 RC low-pass filters with cutoff frequency of 100 kHz. Ribbon cables connect the inputs of these small boards to a routing board, which maps the 16 outputs of the DAC board to some of the DC electrodes and short the rest of the DC electrodes to the ground.

In our experimental setup, the 369.5 nm lasers are generated either by doubling a 739 nm pump laser or directly from external cavity diode laser system, and the wavelength of those lasers are stabilized either by locking to an Iodine cell similar to the procedure explained in Olmschenk *et al.* [10] or by a feedback loop implemented with a wavelength meter. The 399 nm laser and the 935 nm laser are also stabilized by the same wavelength meter. The instantaneous linewidths of all the lasers are specified to be less than 1 MHz, but because of the slow feedback loop, the lasers are stabilized within a range of 5 MHz offset from the target frequencies.

To trap $^{171}Yb^{+}$ ions and manipulate them for simple quantum operations such as Rabi oscillation shown in **Figure 10**, we set up laser systems as shown in **Figure S5**. The frequency of the 369.5 nm laser was set to f_1 = 811.28887(1) THz that is 210 MHz red-detuned from our measured resonant frequency of $^2P_{1/2}|F=0,m_F=0\rangle \leftrightarrow {}^2S_{1/2}|F=1,m_F=0\rangle$ transition. The frequency of the 935 nm laser was set to f_5 = 320.56925(1) THz which is resonant with $^2D_{3/2}|F=1\rangle \leftrightarrow {}^3D[3/2]_{1/2}|F=0\rangle$ transition and the phase was continuously modulated by a fiber-based electro-optic modulator (EOM) at 3.07 GHz to generate a sideband frequency resonant with $^2D_{3/2}|F=2\rangle \leftrightarrow {}^3D[3/2]_{1/2}|F=1\rangle$ transition.

Doppler cooling of the $^{171}Yb^{+}$ ion requires an additional frequency resonant with the $^2S_{1/2}|F=0\rangle \leftrightarrow {}^2P_{1/2}|F=1\rangle$ transition, and it was generated by the second-order sideband generated by a resonant EOM1 driven at 7.37 GHz. An acousto-optic modulator (AOM1) adds 200 MHz to all the frequency components as shown in **Figure S6** so that both the carrier frequency (f_1) and the second-order sideband are red-detuned by 10 MHz from the corresponding transitions. The AOM1 and AOM2 are used to shift the frequency by different amounts as well as to switch the lasers on and off at sub-microsecond timing.

The $^2S_{1/2}|F=0,m_F=0\rangle$ state and the $^2S_{1/2}|F=1,m_F=0\rangle$ state of the $^{171}Yb^{+}$ ion are defined as $|0\rangle$ and $|1\rangle$ respectively. To initialize the quantum bit (qubit) to $|0\rangle$, the ion was optically pumped into $^2S_{1/2}|F=0,m_F=0\rangle$ by using a frequency resonant with $^2S_{1/2}|F=1\rangle \leftrightarrow {}^2P_{1/2}|F=1\rangle$ transition, which was generated by driving the EOM2 at 2.105 GHz and adding 200 MHz with AOM1 in **Figure S6**.

The quantum state of $^{171}Yb^{+}$ qubit can be rotated around the Bloch sphere in a rotating frame by applying a microwave of 12.643 GHz which is resonant with $^2S_{1/2}|F=0,m_F=0\rangle \leftrightarrow {}^2S_{1/2}|F=1,m_F=0\rangle$ transition. The rotation axis in the Bloch sphere is determined by the relative phase of the microwave and the rotation angle is proportional to the product of the microwave amplitude and the duration T_{rot}. In our setup, the microwave was applied using a horn antenna with 10 dB gain.

To measure the qubit value after each rotation, only AOM2 was turned on so that the frequency of the 369.5 nm laser is resonant with only $^2S_{1/2}|F=1\rangle \leftrightarrow {}^2P_{1/2}|F=0\rangle$. If the

quantum state of the qubit collapses to $|0\rangle = {}^2S_{1/2}|F=0\rangle$, the selection rule allows only ${}^2S_{1/2}|F=0\rangle \leftrightarrow {}^2P_{1/2}|F=1\rangle$ transition, and because of the large detuning (14.75 GHz) from the incident light, probability of making that transition is very small and thus the $^{171}Yb^+$ ion will rarely scatter any photon. On the other hand, if the quantum state of the qubit collapses to $|1\rangle = {}^2S_{1/2}|F=1\rangle$, the $^{171}Yb^+$ ion will scatter multiple photons from the incident light through cycling transitions. Therefore $|0\rangle$ and $|1\rangle$ states can be distinguished by counting the scattered photons with a photomultiplier tube (PMT) for a fixed duration T_{detect}.

To demonstrate the Rabi oscillation, after initializing the qubit to $|0\rangle$ a resonant microwave is applied for a variable duration T_{rot}, and then the resulting quantum state of the qubit is measured. Note that because of the probabilistic nature of quantum mechanics, each measurement can give only either $|0\rangle$ or $|1\rangle$. Therefore, to find out the populations of $|0\rangle$ and $|1\rangle$ states for a given value T_{rot}, the sequence summarized in **Table S1** should be repeated multiple times so that the probability of measuring $|1\rangle$ state can be estimated from the statistics of the measured data. For example, to obtain the data in **Figure 10**, T_{cool} = 1000 μs, T_{init} = 100 μs, T_{detect} = 1500 μs were used, and T_{rot} was varied from 0 μs to 5000 μs with a step size of 50 μs and for each data point, the experimental sequence in **Table S1** was repeated 5000 times.

To synchronize the timings of the radio-frequency (RF)/microwave switch operation and the photon counter, control signals are generated by an FPGA board programmed by a custom Verilog code and parameter setting and data collection are done by home-grown programs based on either Python or Matlab in our system. Note that open-source software packages designed for ion trap experiments are also available[11].

S.7. Determination of DC voltage sets

This section describes a methodology for designing a DC voltage set with a simple electrode layout including three pairs of outer DC electrodes and a pair of inner DC electrodes shown in **Figure S7**, which can confine the ions along the axial direction (*z*-axis) and tilt the principal axes of the total potential in the radial direction (*xy*-plane). The design sequence starts with the electric field simulations. We use a boundary element method (BEM) in our simulations, but finite element methods (FEM) can also be used. First, electric fields and potentials are calculated for each electrode under the assumption that 1 V is applied to that electrode while the rest of the electrodes are set to 0 V. Then the DC electric potential can be obtained by a linear combination of the individual electric potentials scaled by the actual DC voltages used. The ponderomotive potential experienced by the trapped ions is given by $\phi_{pp}(\mathbf{r}) = e|E(\mathbf{r})|^2/4m\Omega^2$, where e, m, Ω, $\mathbf{r}$, and $E(\mathbf{r})$ represent elementary charge, ion mass, the angular frequency of the applied RF voltage, the position vector and the amplitude of the electric field generated by the RF voltage applied to the RF electrodes, respectively. Then the total potential is simply the sum of the ponderomotive potential and the DC potential.

Figure S7 shows labels for the DC electrodes for the following discussion. Eight DC electrodes are grouped into outer-corner electrodes (LT, LB, RT, RB), outer-center electrodes (LC, RC), and inner electrodes (LI, RI). To utilize the reflection symmetry of the trap geometry with respect to the *yz*-plane at the middle of the trap, the voltages applied to each group will be decomposed into symmetric and asymmetric components. For example, we can apply a symmetric voltage V_{SO} to the outer-corner electrodes, meaning that $V_{LT} = V_{LB} = V_{SO}$ and $V_{RT} = V_{RB} = V_{SO}$. Then, the direction of the generated electric field at the middle of the

trap (RF null) will be parallel to the y-axis. The amplitude of that field is $V_{SO}E_{ySO}$, where E_{ySO} is the amplitude when V_{SO} = 1 V. On the other hand, if we apply an asymmetric voltage V_{AO} to the same group, meaning that $V_{LT} = V_{LB} = V_{AO}$ and $V_{RT} = V_{RB} = -V_{AO}$, then the generated electric field at the RF null, $V_{AO}E_{xAO}$, will now be parallel to the *x*-axis. Symmetric voltages for outer-center electrodes group (V_{SC}) and for inner electrodes group (V_{SI}) can be similarly defined, which will generate $V_{SC}E_{ySC}$ and $V_{SI}E_{ySI}$ at the RF null respectively. All these symmetric voltages will create electrical fields that are pointing in the *y*-direction. Similarly, asymmetric voltages for outer-center electrodes group (V_{AC}) and for inner electrodes group (V_{AI}) will generate $V_{AC}E_{xAC}$ and $V_{AI}E_{xAI}$ respectively, and they will be parallel to the *x*-axis. To minimize micromotion caused by non-zero DC fields at the RF null[12], the DC fields caused by the outer-corner electrodes group and the outer-center electrodes group must be cancelled by the DC fields generated from the inner electrodes group, namely $V_{SO}E_{ySO} + V_{SC}E_{ySC} + V_{SI}E_{ySI} = 0$ and $V_{AO}E_{xAO} + V_{AC}E_{xAC} + V_{AI}E_{xAI} = 0$.

For our setup, the voltages of the outer electrodes shown in **Figure 4** were adopted from previous experiments using a trap chip with similar dimensions[13], and V_{SI} and V_{AI} were calculated by the method explained above. It is worth mentioning that the symmetric voltages (V_{SO}, V_{SC}) of the outer electrodes contributes heavily to the confining potential along the axial direction (*z*-axis), so they can be adjusted to achieve a desired secular frequency along the axial direction. For secular frequencies in the radial direction, on the other hand, one can vary the RF voltage to achieve the desired values. The asymmetric voltages (V_{AO}, V_{AC}) at the outer electrodes contribute to the tilting of the radial principal axes in the *xy*-plane. For optimal cooling process, tilt angle near 45 degrees is desired. During such adjustment process, output range of the DC voltage source may become the main constraint, and it is recommended that all the final voltages be at least 1 V less than the maximally allowed values so that there will always be some margin left for voltage adjustments as explained in S.8.

S.8. Minimization of micromotion amplitude

After the initial trapping of a single ion, electrical voltages should be adjusted to extend the lifetime of the ion. The voltages for the DC electrodes are generally chosen based on the simulation of the electric field inside the trapping region[5], but the actual setup always has some deviations from the ideal calculation, which should be compensated by the DC voltage adjustment. Generally, the location of RF null where the RF field becomes zero does not coincide with the location of DC null, and this offset causes a micromotion of trapped ion[14]. To minimize the micromotion, we generally use the following three different methods to detect the offset.

Method 1: When there is an offset between the RF null and the DC null in the *xy*-plane, the ion gets trapped where the ponderomotive force and the electrostatic force from the DC potential are balanced. Therefore, when the amplitude of the RF voltage is changed, even though the locations of both nulls are fixed, the trapping position is shifted. When there is a large offset between the RF and DC null, this shift can be observed by a high-resolution imaging lens and therefore this method is used for coarse adjustment of the DC voltages.

Method 2: When a micromotion exists, the velocity of the ion changes sinusoidally within one period of the applied RF frequency, and there is a time correlation between the phase of

the RF signal and the velocity of the ion. Because of Doppler shift, the amount of detuning of the 369.5 nm laser from the atomic resonance depends on the velocity of the ion along the propagation axis of the laser. Therefore, the scattering probability of the laser depends on the phase of the RF signal, and when the micromotion amplitude is nonzero, a plot of the scattering probability as a function of the RF phase shows a sinusoidal curve whose amplitude has a positive correlation with the amplitude of the micromotion. To obtain the scattering rate, a PMT with a 200-μm diameter pinhole and a flip-mirror are used as shown in **Figure 6(c)**. To measure the time-correlation, the trigger output of the RF generator is connected to the start trigger of an event timer and the output of the PMT is connected to the stop trigger of the event timer. Then a histogram of the photon counts with respect to time intervals shows the scattering probability as a function of the RF phase, and as the micromotion is minimized, the variation of the photon counts as a function of the time interval gets reduced[14].

Method 3: Method 2 can detect the micromotion only in the *xz*-plane, but to achieve optimal trapping conditions, the micromotion along *y*-axis should also be minimized. Similar to the shift of the trapping position explained in Method 1, if the amplitude of the RF voltage is modulated at frequency ω, the trapped ion will also be wiggled at the same frequency, and when ω is resonant with one of the radial secular frequencies, the corresponding secular motion gets amplified[12,15], which in turn leads to the change in the scattering rate. Therefore, by monitoring the amount of change in the brightness of the ion when the RF voltage is modulated at its secular frequencies, the DC null can be adjusted to coincide with the RF null.

S.9. Measurement result of Rabi oscillation

To obtain the Rabi oscillation data in **Figure 10**, the experimental sequence in **Table S1** was repeated 5,000 times for each data point. The data was fitted to a sinusoidal curve centered at 50% with the amplitude as a free parameter, and Rabi frequency of 636.15(12) Hz and the visibility of 99.6(2) % were obtained from the fitted curve. To estimate the coherence time, two different methods were tried. When the Rabi flopping was continued up to 100 ms, the visibility dropped down to ~60 %, and when we measured Ramsey fringe[15], the visibility dropped down to ~60 % after 300 ms. However, when we applied multiple spin-echo pulses at 5-ms interval, the visibility of Ramsey fringe stayed above 80 % even after 1 second and beyond that interval, measurement of the visibility was mainly limited by the reduced photon scattering rate caused by heating of the ion. We believe that the visibility of the repeated Rabi flopping was mainly limited by the intensity fluctuation of the applied microwave and the visibility of the Ramsey fringe measurement was limited by the fluctuation of the magnetic field.

FIGURE & TABLE:

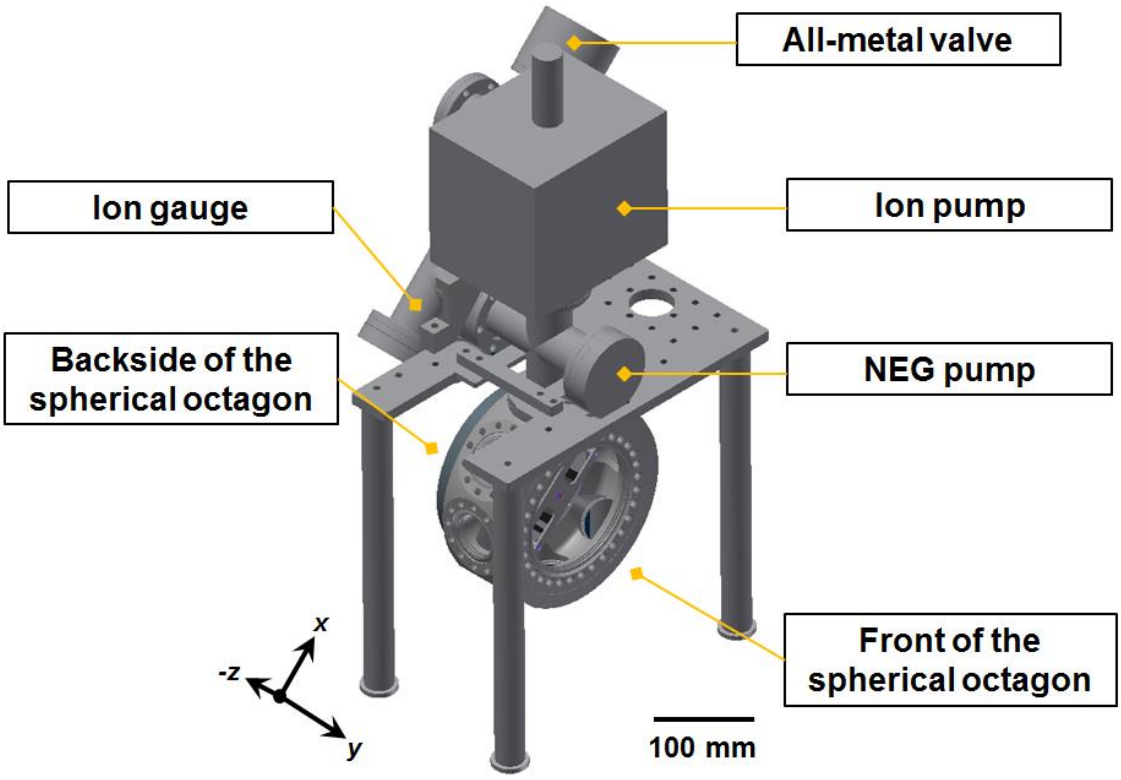

Figure S1. Overall design of the ultra-high vacuum (UHV) chamber. It is composed of one ion pump, one non-evaporable getter (NEG) pump, one ion gauge, one all-metal valve, and a spherical octagon. All the viewports are omitted for clarity.

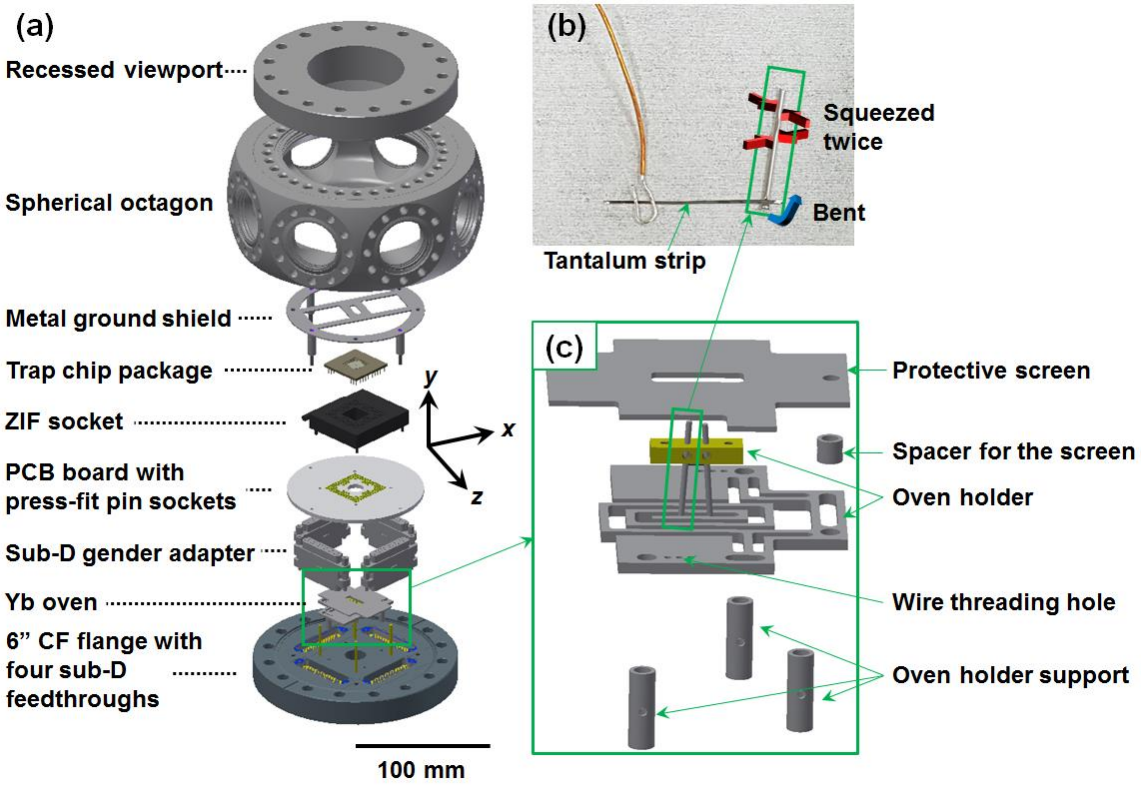

Figure S2. Design of the spherical octagon assembly. (a) Illustration of the internal structure. A ZIF socket is mounted on a PCB[4] through press-fit type pin sockets. The PCB board is fixed to a 6" CF flange with multi-pin feedthroughs via four 25 D-sub gender adapters made of polyether ether ketone (PEEK). A metal ground shield is added to minimize potential disturbance from any stray charges trapped on the front viewport. **(b)** Picture of a metal tube, a Tantalum strip, and a Kapton wire. One end of the tube is bent to prevent backward spray of Yb evaporation as shown with blue arrows in **Fig. S2(b)**, and the middle of the oven is squeezed in two perpendicular directions along the tube to prevent small Yb pieces from falling out as shown with red arrows in **Fig. S2(b)**. **(c)** Magnified view of the oven holder package. The top shield is added to prevent a short circuit between the PCB traces that can result from the evaporation of the filament material.

(a)

Atomic weight	170	171	172	173	174	176
Expected natural abundance	3.0%	14.3%	21.8%	16.1%	31.8%	12.8%

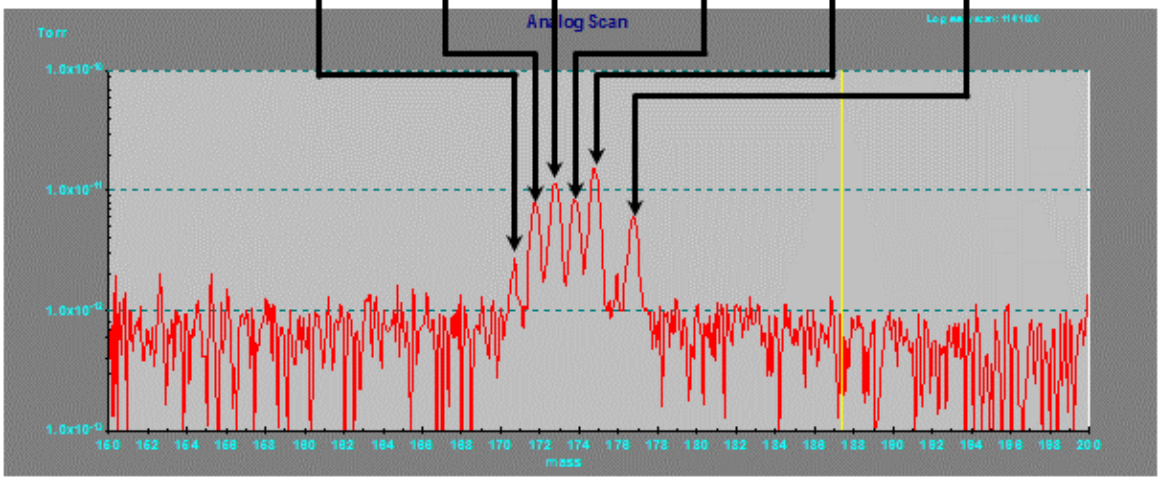

(b)

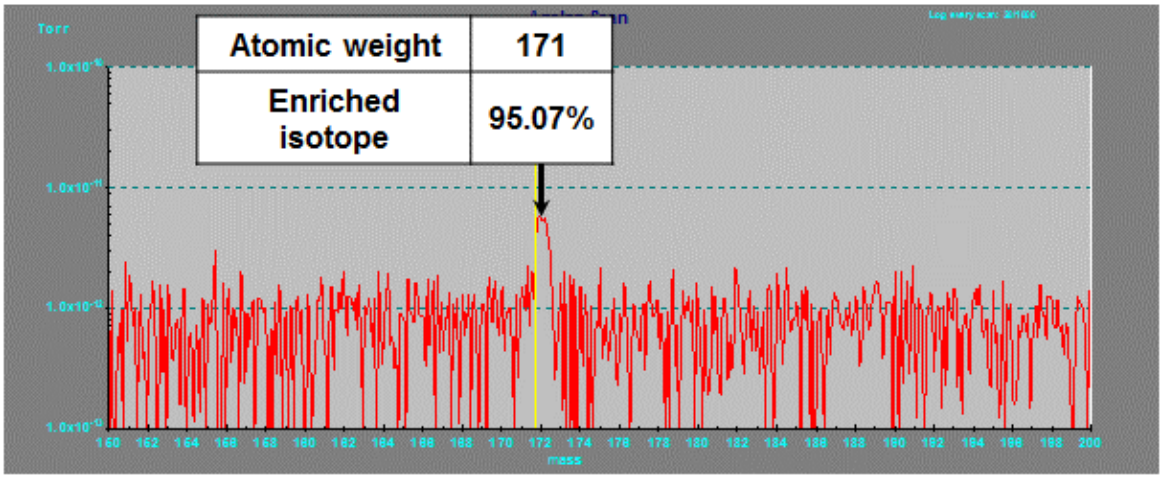

Figure S3. Measurement of Yb isotopes with RGA. (a) Mass spectrum of the evaporation from the oven filled with naturally occurring Yb. Measured spectrum shows a similar distribution with the expected natural abundance which is also summarized in the table. **(b)** Mass spectrum of the evaporation from the oven filled with isotopically enriched ^{171}Yb. Only a single peak at 171 is visible. The percentage of the enriched isotope is based on the datasheet from the supplier. Note that the data were taken without any calibration and therefore both plots have constant offset of one atomic mass unit.

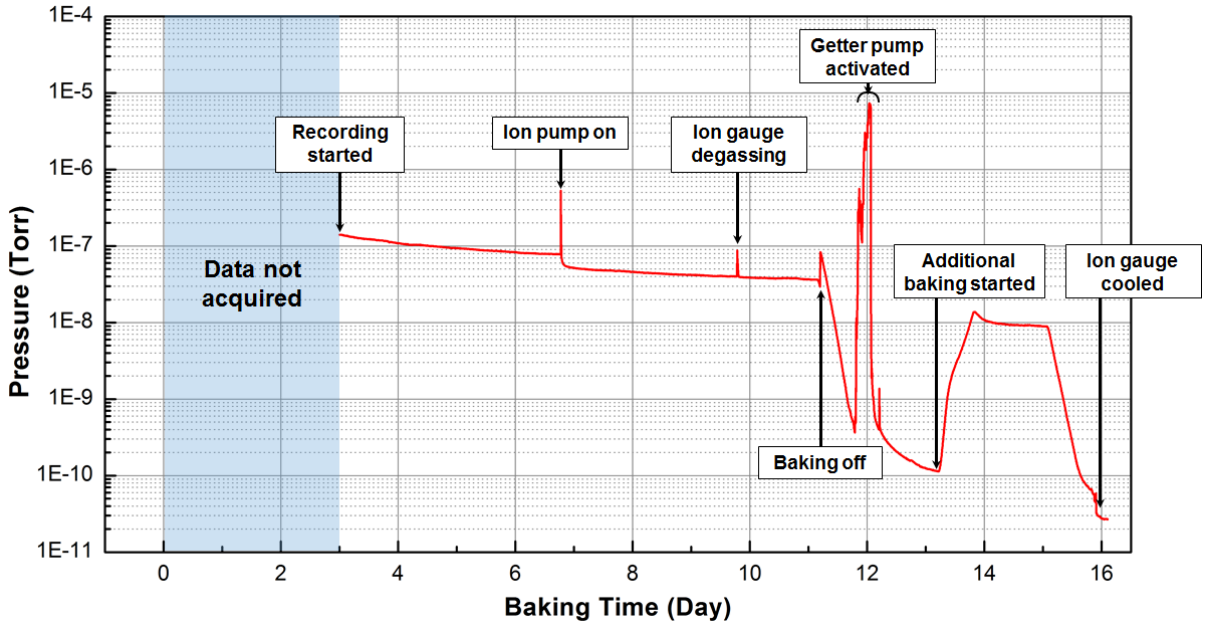

Figure S4. Log of the vacuum pressure measured with an ion gauge during a long period of chamber baking.

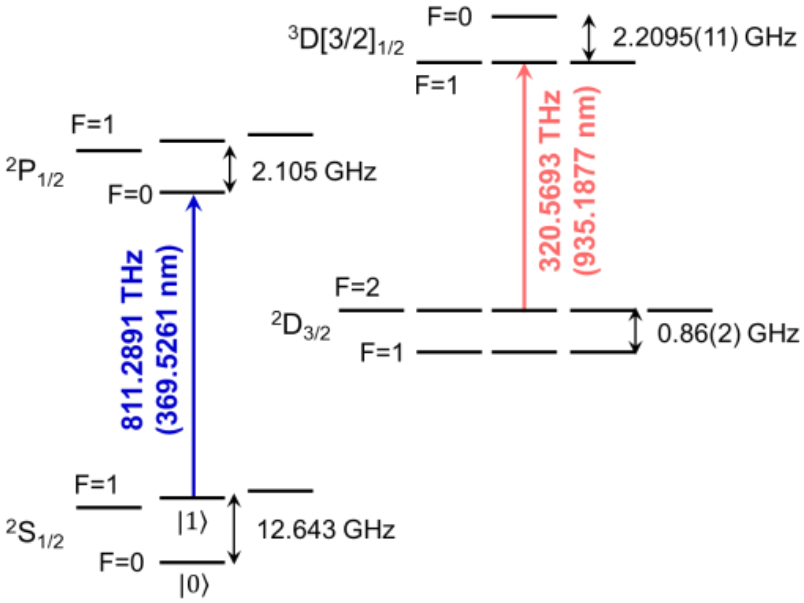

Figure S5. A simplified energy level diagram of the $^{171}Yb^+$ ion.

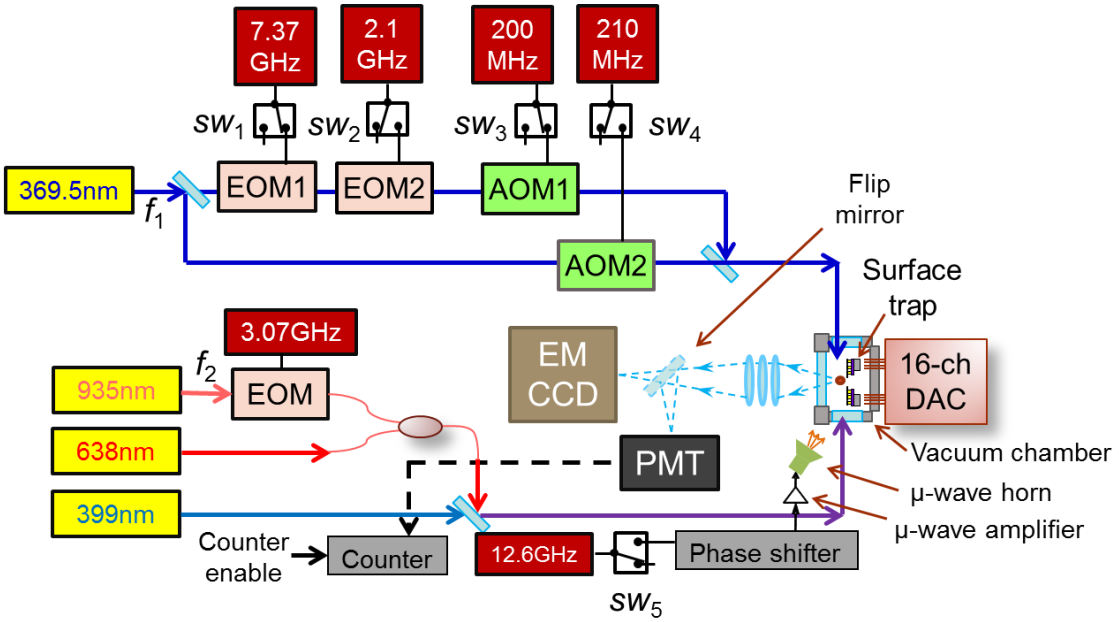

Figure S6. The experimental setup for trapping of the $^{171}Yb^{+}$ qubits and controlling their quantum states.

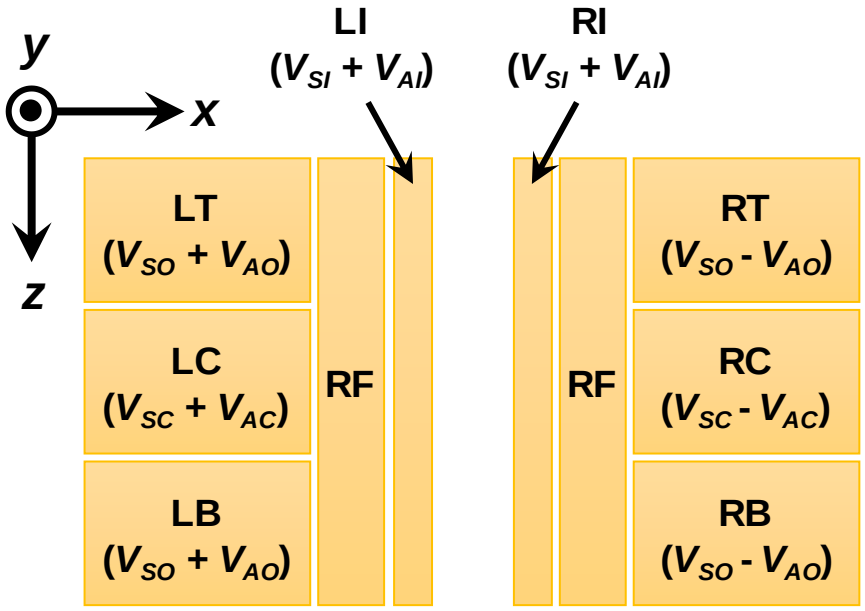

Figure S7. Simplified layout of the DC electrodes.

Table S1. Summary of a single experimental sequence for Rabi oscillation measurement.

Step	Duration	sw_1	sw_2	sw_3	sw_4	sw_5	Counter enable
1. Doppler cooling	T_{cool}	on	off	on	off	off	off
2. Initialization	T_{init}	off	on	on	off	off	off
3. Rotation in Bloch sphere	T_{rot}	off	off	off	off	on	off
4. State detection	T_{detect}	off	off	off	on	off	on

REFERENCES:

1. Niedermayr, M., *et al.* Cryogenic surface ion trap based on intrinsic silicon. *New Journal of Physics* **16** (11), 113068. doi:10.1088/1367-2630/16/11/113068 (2014).
2. Wilpers, G., See, P., Gill, P., Sinclair, A. G. A compact UHV package for microfabricated ion-trap arrays with direct electronic air-side access. *Applied Physics B* **111** (1), 21-28. doi:10.1007/s00340-012-5302-410 (2013).
3. Brown, K. R., Clark, R. J., Labaziewicz, J., Richerme, P., Leibrandt, D. R., Chuang, I. L. Loading and characterization of a printed-circuit-board atomic ion trap. *Physical Review A* **75** (1), 015401. doi: 10.1103/PhysRevA.75.015401 (2007).
4. Graham, R. D., Chen, S. P., Sakrejda, T., Wright, J., Zhou, Z., Blinov, B. B. A system for trapping barium ions in a microfabricated surface trap. *AIP Advances* **4** (5), 057124. doi:10.1063/1.4879817 (2014).
5. Hong, S., Lee, M., Cheon, H., Kim, T., Cho, D. I. Guidelines for designing surface ion traps using the boundary element method. *Sensors* **16** (5), 616. doi:10.3390/s16050616 (2016).
6. Olmschenk, S. *Quantum teleportation between distant matter qubits*, Doctoral dissertation. (2009).
7. Berkeland, D. J., Boshier, M. G. Destabilization of dark states and optical spectroscopy in Zeeman-degenerate atomic systems. *Physical Review A* **65** (3), 033413. doi:10.1103/PhysRevA.65.033413 (2002).
8. Kleinert, M., Dahl, M. E. G., Bergeson, S. Measurement of the Yb I $^1S_0$–$^1P_1$ transition frequency at 399 nm using an optical frequency comb. *Physical Review A* **94** (5), 052511. doi:10.1103/PhysRevA.94.052511 (2016).
9. Mount, E., *et al.* Scalable digital hardware for a trapped ion quantum computer. *Quantum Information Processing* **15** (12), 5281–5298. doi:10.1007/s11128-015-1120-z (2016).
10. Olmschenk, S., Younge, K. C., Moehring, D. L., Matsukevich, D. N., Maunz, P., Monroe, C. Manipulation and detection of a trapped Yb^+ hyperfine qubit. *Physical Review A* **76** (5), 052314. doi:10.1103/PhysRevA.76.052314 (2007).
11. *NIST's Advanced Real-Time Infrastructure for Quantum Physics (ARTIQ).* Retrieved from https://m-labs.hk/artiq (2017, Mar. 14)
12. Ibaraki, Y., Tanaka, U., Urabe, S. Detection of parametric resonance of trapped ions for micromotion compensation. *Applied Physics B* **105** (2), 219–223. doi:10.1007/s00340-011-4463-x (2011).
13. Stick, D., et al. Demonstration of a microfabricated surface electrode ion trap. *arXiv preprint* arXiv:1008.0990. (2010).
14. Berkeland, D. J., Miller, J. D., Bergquist, J. C., Itano, W. M., Wineland, D. J. Minimization of ion micromotion in a Paul trap. *Journal of Applied Physics* **83** (10), 5025-5033. doi: 10.1063/1.367318 (1998).
15. Mount, E., et al. Single qubit manipulation in a microfabricated surface electrode ion trap. *New Journal of Physics* **15** (9), 093018. doi:10.1088/1367-2630/15/9/093018 (2013).